Monthly Notices of the ROYAL ASTRONOMICAL SOCIETY

MNRAS **527,** 10239–10253 (2024) https://doi.org/10.1093/mnras/stad3845
Advance Access publication 2023 December 20

OGLE-BLAP-009 – a case study for the properties and evolution of blue large-amplitude pulsators

Corey W. Bradshaw,[1★] Matti Dorsch,[2,3] Thomas Kupfer,[1,4] Brad N. Barlow,[5,6] Uli Heber,[3] Evan B. Bauer,[7] Lars Bildsten[8] and Jan van Roestel[9]

[1]*Department of Physics and Astronomy, Texas Tech University, Lubbock, TX 79409, USA*
[2]*Institut für Physik und Astronomie, Universität Potsdam, D-14476 Potsdam-Golm, Germany*
[3]*Dr. Karl Remeis-Observatory & ECAP, Astronomical Institute, Friedrich-Alexander University Erlangen-Nuremberg (FAU), D-96049 Bamberg, Germany*
[4]*Hamburger Sternwarte, University of Hamburg, Gojenbergsweg 112, D-21029 Hamburg, Germany*
[5]*Department of Physics and Astronomy, High Point University, High Point, NC 27268, USA*
[6]*Department of Physics and Astronomy, University of North Carolina at Chapel Hill, Chapel Hill, NC 27599, USA*
[7]*Center for Astrophysics|Harvard & Smithsonian, Cambridge, MA 02138, USA*
[8]*Kavli Institute for Theoretical Physics, University of California, Santa Barbara, CA 93106, USA*
[9]*Anton Pannekoek Institute for Astronomy, University of Amsterdam, NL-1090 GE Amsterdam, The Netherlands*

Accepted 2023 December 7. Received 2023 December 4; in original form 2023 September 29

ABSTRACT

Blue large-amplitude pulsators (BLAPs) make up a rare class of hot pulsating stars with effective temperatures of ≈30 000 K and surface gravities of 4.0–5.0 dex (cgs). The evolutionary origin and current status of BLAPs is not well understood, largely based on a lack of spectroscopic observations and no available mass constraints. However, several theoretical models have been proposed that reproduce their observed properties, including studies that identify them as pulsating helium-core pre-white dwarfs (He-core pre-WDs). We present here follow-up high-speed photometry and phase-resolved spectroscopy of one of the original 14 BLAPs, OGLE-BLAP-009, discovered during the Optical Gravitational Lensing Experiment. We aim to explore its pulsation characteristics and determine stellar properties such as mass and radius in order to test the consistency of these results with He-core pre-WD models. Using the mean atmospheric parameters found using spectroscopy, we fit a spectral energy distribution to obtain a preliminary estimate of the radius, luminosity, and mass by making use of the *Gaia* parallax. We then compare the consistency of these results to He-core pre-WD models generated using Modules for Experiments in Stellar Astrophysics, with predicted pulsation periods implemented using GYRE. We find that our mass constraints are in agreement with a low-mass He-core pre-WD of ≈0.30 $M_{\odot}$.

Key words: asteroseismology – stars: evolution – stars: individual: OGLE-BLAP-009 – stars: oscillations (including pulsations).

1 INTRODUCTION

Blue large-amplitude pulsators (BLAPs) comprise a class of hot variable stars that reside in a region of the Hertzsprung–Russell (HR) diagram, below the main sequence, that is typically populated with hot subdwarf stars (sdOBs). BLAPs have spectral classifications of O or B and show periodic brightness variations on the time-scale of 10–40 min with amplitudes of 0.2–0.4 mag (Pietrukowicz et al. 2017; Pigulski, Kotysz & Kołaczek-Szymański 2022; Ramsay et al. 2022). Originally, 14 of these objects were discovered as a part of the Optical Gravitational Lensing Experiment (OGLE) survey of the Galactic Bulge and Disc (Udalski, Szymański & Szymański 2015). These stars have light curves similar to those found in fundamental mode pulsating Cepheid and RR-Lyrae stars but with higher effective temperatures ($T_{\rm eff}$) of ≈30 000 K and surface gravities ($\log(g)$) of ≈4.5 (Pietrukowicz et al. 2017). Since then, four objects were found from the Zwicky Transient Facility (ZTF) at low Galactic latitudes that exhibit large-amplitude pulsations with similar $T_{\rm eff}$ but higher $\log(g)$ of ≈5.4 and shorter pulsation periods in the range 3–8 min. These objects were then classified as high-gravity BLAPs (Kupfer et al. 2019). Ramsay et al. (2022) reported the discovery of four BLAPs as part of the OmegaWhite survey, one of which is OGLE-BLAP-009, confirming its previously observed parameters. All of their BLAPs have properties consistent with those reported by Pietrukowicz et al. (2017). Additionally, Pigulski, Kotysz & Kołaczek-Szymański (2022) and Lin et al. (2023) each confirmed a BLAP as component of a binary pair. These discoveries constitute the only two BLAPs to be found in a binary system. More BLAP candidates have been proposed by McWhirter & Lam (2022) through cross-matching sources meeting colour-corrected selection criteria in *Gaia* DR2 (Gaia Collaboration 2016, 2018) to light curves from ZTF DR3. The position of BLAPs and high-gravity BLAPs on the HR diagram and corresponding effective temperatures are similar to that

★ E-mail: Corey.Bradshaw@ttu.edu

of B-type hot-subdwarf (sdB) stars but with lower surface gravities in the case of BLAPs (see Heber 1986, 2009, 2016).

The evolutionary history of these objects is not fully understood, and several scenarios have been proposed. Along with the initial discovery of BLAPs, Pietrukowicz et al. (2017) suggested two models that may reproduce their observed properties. The first is that of a star in the helium-core (He-core) burning phase with an inflated hydrogen envelope and a mass of $\approx$1 $M_\odot$, which may occur in hot stars as a result of significant mass-loss of about 75 per cent. The second case is that of a stripped red giant, whose energy is produced by a hydrogen-burning shell above a degenerate helium-core resulting in a pre-white dwarf (He-core pre-WD) of $\approx$0.30 $M_\odot$. Both scenarios require significant mass-loss, which establishes a connection to sdB stars; however, this requirement is less extensive in the second case and was considered to be more likely (Pietrukowicz et al. 2017).

Several theoretical investigations into pulsating He-core pre-WDs have been performed. Córsico et al. (2016) found that non-radial p, g, and $p - g$ mixed pulsations can occur in He-core pre-WDs due to the $\kappa - \gamma$ mechanisms. Expanding on this, Romero et al. (2018) and Córsico et al. (2018) found that evolutionary tracks of the hot counterparts to these pre-extremely low-mass (pre-ELM) white dwarfs with masses between 0.27 and 0.37 $M_\odot$ can reproduce the observed $T_{\rm eff}$ and $\log(g)$ of BLAPs. The pulsation periods of these models were best described by low-order radial-modes or high-order g-mode pulsations due to the κ-mechanism. Byrne & Jeffery (2018, 2020) reported that the fundamental radial mode can be excited when including radiative levitation of iron-group elements in post-common envelope evolution models that result in the formation of a low-mass He-core pre-WD of $\approx$0.31 $M_\odot$ pulsating as a result of the κ-mechanism.

Kupfer et al. (2019), in the initial discovery of high-gravity BLAPs, tested their observed properties with models developed using the Modules for Experiments in Stellar Astrophysics (MESA) stellar evolution code for both He-core pre-WDs as well as low-mass He-core burning stars with thin hydrogen envelopes of various masses. These tracks also included adiabatic pulsation periods calculated for the fundamental and first-overtone radial modes. They found that the $T_{\rm eff}$ and $\log(g)$ of these stars could be represented by both models, but the observed periods more closely resembled He-core pre-WDs pulsating in the fundamental radial mode. Using the dynamical frequency for these models in order to calculate radius and mass, they found that the four high-gravity BLAPs had masses between 0.19 and 0.35 $M_\odot$ with radii of 0.10–0.22 $R_\odot$. They concluded that their objects favoured the low-mass He-core pre-WD models over the more massive He-core burning models (Kupfer et al. 2019).

The proposed evolutionary status of a pre-WD leads to the possibility of a binary evolution channel being responsible for the production of BLAPs. However, only two BLAPs have been discovered with a binary companion (Pigulski, Kotysz & Kołaczek-Szymański 2022; Lin et al. 2023). Pigulski, Kotysz & Kołaczek-Szymański (2022) identified a BLAP as the secondary component in the binary system HD 133729, with a late B-type main-sequence primary and a 23.084 33 d orbital period. Lin et al. (2023) discovered a BLAP as part of the Tsinghua University – Ma Huateng Telescopes for Survey (TMTS), TMTS-BLAP1, in an approximately 1500 d orbital period around a dwarf companion using light-traveltime effects. A binary population synthesis study performed by Byrne, Stanway & Eldridge (2021) found that BLAPs can in fact be produced through mass stripping of their progenitor via common envelope evolution (CEE) or stable Roche lobe overflow (RLOF). The lack of BLAPs without observed binary companions is therefore puzzling. Meng et al. (2020) showed that He-core burning survivors of Type Ia supernovae with masses of $\approx$0.75 $M_\odot$ can reproduce the observed properties of BLAPs, leading to a possible explanation for the lack of observable companions. These proposed evolutionary pathways suggest that BLAPs may serve an important role in investigating stages of binary evolution.

Hot subdwarf models for He-core and He-shell-burning stars have also been studied as a potential evolutionary scenario for BLAPs. Wu & Li (2018) found that He-core burning subdwarfs with masses in the range of 0.70–1.10 $M_\odot$ reproduced observed spectroscopic properties as well as reported rates of period change. This range of masses is consistent with findings from Meng et al. (2020). Investigations carried out by Xiong et al. (2022) showed that He-shell-burning stars with core masses in the range of 0.45–0.50 $M_\odot$ can reproduce observed BLAP properties while these stars with higher core masses of 0.75–1.0 $M_\odot$ were unable to reproduce these properties.

It remains an open question as to which evolutionary state BLAPs currently reside in and if they all share similar origins. Currently there are no mass or radius estimates for any of the known BLAPs, excluding the high-gravity BLAPs. Additional observations that aid in constraining the physical properties of these stars will help to determine their proper status. We present a detailed follow-up analysis of one particularly interesting BLAP, OGLE-BLAP-009. This object was initially reported by Macfarlane et al. (2017) as a peculiar δ Scuti-type pulsating star found in the OmegaWhite survey and then independently found and formally classified as a BLAP as part of the OGLE survey of the Galactic Bulge and Disc. This star has a reported period of 31.94 min from OGLE photometry with a $T_{\rm eff}$ of 31 800 $\pm$ 1400 K and a $\log(g)$ of 4.40 $\pm$ 0.18 from long-exposure (300 s) low-resolution ($R \approx 800$) spectroscopy obtained using Gemini (Pietrukowicz et al. 2017). In this study, we aim to estimate the fundamental properties of this star and constrain its evolutionary history. Data from time-series photometry and spectroscopy were used to derive a precise period, $T_{\rm eff}$ and $\log(g)$ as well as investigate the stellar pulsations and search for radial velocity signatures of a binary companion. To obtain an initial estimate of the mass and radius we fit a spectral energy distribution and combine the results with the *Gaia* EDR3 parallax measurement. We then compare these results to He-core pre-WD models developed using MESA and derive a mass and radius using a dynamical frequency calculation from GYRE predicted pulsation periods, to test this evolutionary channel.

2 OBSERVATIONS

Follow-up high-speed photometry was performed using the 2.1 m (82 inch) Otto Struve Telescope with the ProEM frame-transfer CCD detector located at McDonald Observatory in Fort Davis, Texas. Data was taken over three nights in 2021 July in both g and r bands using 8-s exposure times, resulting in 1100 g-band exposures and 891 r-band exposures. Data reduction was performed using standard IRAF pipelines. All frames were bias-subtracted and flat-fielded.

Phase-resolved spectroscopy was obtained using the Keck telescopes in Hawaii. The Echellette Spectrograph and Imager (ESI; Sheinis et al. 2002) was used to obtain fifteen 2-min exposures at a medium resolution ($R \approx 6000$) in 2020 July covering 1.18 pulsation cycles. An additional eight 2-min exposures were taken in 2021 June which covered 0.64 pulsation cycles. The spectra were reduced using the MAKEE[1] pipeline following the standard procedure:

[1] https://sites.astro.caltech.edu/~tb/makee/

Table 1. Complete list of data used in the analysis, including both time-series photometry and spectroscopy.

Photometry	Date	Filter	Exp. time (s)	Exps.
OGLE 3 & 4	2001–2016	*V*, *I*	–	2448
2.1m/Pro-EM	2021 July 9	*g*'	8	1100
2.1m/Pro-EM	2021 July 10	*r*'	8	644
2.1m/Pro-EM	2021 July 11	*r*'	8	247
Spectroscopy	Date	Camera	Exp. time (s)	Exps.
Keck/ESI	2020 July 22	–	120	14
Keck/ESI	2021 June 7	–	120	8
Keck/LRIS	2021 Sept. 11	Blue	120	16

bias subtraction, flat fielding, sky subtraction, order extraction, and wavelength calibration.

The Low-Resolution Imaging Spectrometer (LRIS; Oke et al. 1995) was also used to collect sixteen 2-min exposures at a low resolution ($R \approx 1000$) in 2021 September covering 1.23 pulsation cycles. Table 1 lists all the data used in this analysis. Data reduction was performed with the Lpipe pipeline[2] (Perley 2019).

3 RESULTS

3.1 Photometry

Data released from the OGLE 3 & 4 surveys in both *V* and *I* bands, along with high-speed follow-up data obtained from McDonald observatory in the *g* and *r* bands was used in our photometric study of OGLE-BLAP-009. Combining these data together resulted in photometry covering a 20 yr time-span. Using the PERIOD04 module (Lenz & Breger 2005), a Fourier analysis revealed a precise period of 31.935 261 66(4) min. The Fourier spectrum showed a single dominant frequency with several harmonics at integer multiples of this value as a result of the non-sinusoidal waveform. No additional signals were found after subtracting this fundamental frequency, confirming the mono-periodicity found by both Pietrukowicz et al. (2017) and additional follow-up photometry from McWhirter, Lam & Steele (2020). High-cadence data collected in both the *g* and *r* bands from McDonald Observatory were combined and their Fourier spectrum revealed a fundamental period of 31.935 ± 0.002 min. Calculating the individual relative flux amplitudes of each light curve resulted in 0.248 ± 0.003 mag for the *g* band and 0.224 ± 0.003 mag for the *r* band, with higher amplitudes occurring in the *g* band, as expected for radial-mode pulsators. After fitting and subtracting this dominant frequency, no additional signals were found. We also see no photometric indications of a binary companion in the form of eclipses or amplitude modulation from a reflection effect or ellipsoidal modulations. Due to the short baseline of our follow-up photometry, we do not achieve a precision capable of measuring a rate of period change in relation to previous OGLE data that is on the order of those found by Pietrukowicz et al. (2017) (10^{-7} yr^{-1}).

Fig. 1 shows the light curves in the *g* and *r* bands in the top and middle panels, phase-folded on the calculated period of 31.935 261 66(4) min and plotted over two pulsation cycles for visualization, where phase zero is defined from the ephemeris with $t_0 = 0$ d, where we use MBJD for timing measurements. The light curves have a typical sawtooth shape with a fast rise to maximum flux covering ≈27 per cent of the pulsation cycle followed by a slow decay lasting for ≈63 per cent of the cycle. The drop to flux minimum is stalled for ≈10 per cent of the pulsation cycle, between rise and decay, where the flux makes a small 'dip' about its maximum. The light curves from both Pietrukowicz et al. (2017) and McWhirter, Lam & Steele (2020) also show this double-peak feature that is clearly illustrated here in our high-cadence data. There are other BLAPs that show this feature at or near maximum flux as well (see Pigulski, Kotysz & Kołaczek-Szymański 2022; Ramsay et al. 2022) and its potential origins are briefly discussed in Section 4.2. Additionally, $g - r$ colour variability is plotted in the bottom panel, showing that the flux variations are caused by stellar pulsations with bluer colour (i.e. higher temperature) corresponding to the phase of maximum light.

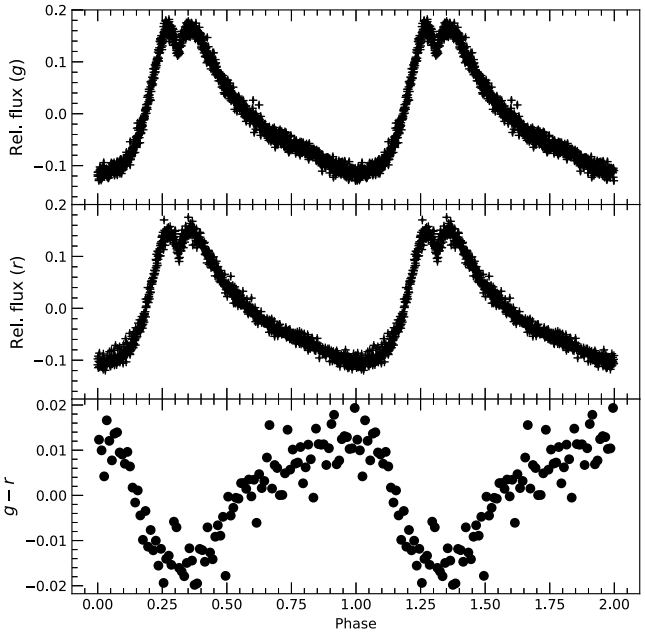

Figure 1. Follow up photometry collected using McDonald Observatory. Top panel: *g*-band light curve, Middle panel: *r*-band light curve, Bottom panel: $g - r$ relative colour variations. All are phase-folded and repeated over two pulsation cycles.

3.2 Spectroscopy

The large photometric variability in the photosphere of this star emphasizes the need for time-series spectroscopy to better understand the atmospheric properties of BLAPs, as they are expected to be highly phase-dependent. Time-series spectroscopy collected from Keck/ESI and Keck/LRIS show large radial velocity (RV), $T_{\rm eff}$, and log (*g*) variability over the pulsation cycle as typically seen in radial-mode pulsators. The large variability in these parameters is caused by physical changes in the star's photosphere such as acceleration, radius expansion and contraction, and temperature changes.

For RV measurements, data collected from Keck/ESI was used, which provides high stability throughout observations, making it the ideal instrument for accurate phase-resolved RV measurements. These were performed by fitting Gaussians, Lorentzians, and polynomials to the hydrogen and helium lines to cover continuum, line, and line core of the individual absorption features using the FITSB2 routine (Napiwotzki et al. 2004). The procedure is described in full detail in Geier et al. (2011). We fitted the wavelength shifts and compared their measurement to the rest wavelengths using a χ^2-minimization.

[2]https://sites.astro.caltech.edu/~dperley/programs/lpipe.html

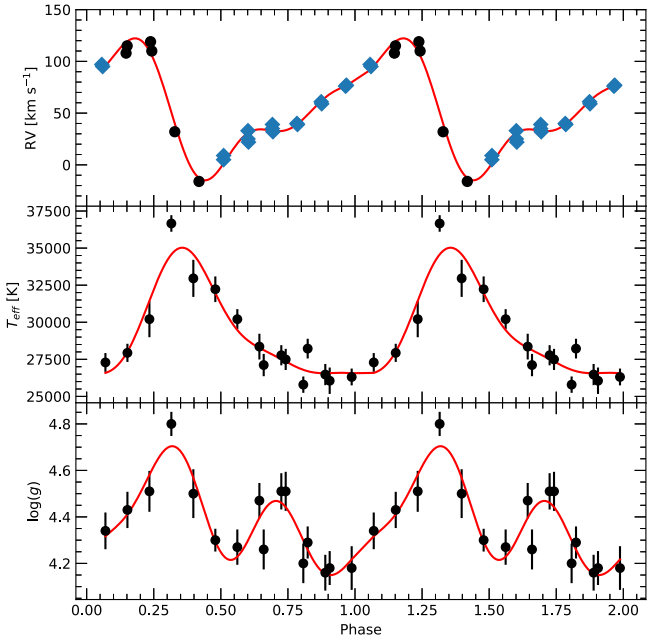

Figure 2. Results from time-series spectroscopy. Top panel: RV measurements from Keck/ESI data sets. Points denoted by blue diamonds represent spectra used in metal abundance calculations. Middle panel: $T_{\rm eff}$ measurements from Keck/LRIS data. Bottom panel: $\log(g)$ measurements from Keck/LRIS data. All curves are phase-folded and repeated over two pulsation cycles, where the red curves are the third order Fourier fitting (equation 1) for each.

High-resolution echelle spectra are not well suited to measure $T_{\rm eff}$ and $\log(g)$ because the broad hydrogen absorption lines span several individual echelle orders and merging of the echelle spectra could introduce systematic errors. Therefore, we used the Keck/LRIS spectra for $T_{\rm eff}$ and $\log(g)$ measurements. We use spectral models computed with TLUSTY/SYNSPEC (Hubeny & Lanz 2017) covering helium dominated atmospheres. The approach and the models are described in detail in Dorsch et al. (2021). This model grid uses Fe and Ni abundances of 1.5 times solar and 10 times solar, respectively. Using the spectral modelling tool SPAS (Hirsch 2009), the individual Keck/LRIS spectra were fitted for $T_{\rm eff}$, $\log(g)$, and helium abundance ($\log(y) = \log(n({\rm He})/n({\rm H}))$ using atmospheric models. The phase-resolved results for $\log(y)$ show no clear variability due to the large uncertainty from fitting individual spectra (see Table B1). We instead perform a full metal abundance analysis using the co-added ESI spectra in Section 3.3. Fig. 2 shows the resulting phase-folded spectroscopic measurements.

In order to uncover the mean values from the resulting RV, $T_{\rm eff}$, and $\log(g)$ curves, it was necessary to fit a model that best represented their non-sinusoidal waveforms. A third order ($n = 3$) Fourier expansion (equation 1) was found to be the best fit to each of the phase-folded curves.

$$\mathrm{RV} = a_0 + \sum_{n=1}^{3} a_n \sin(2\pi n x) + b_n \cos(2\pi n x), \quad (1)$$

where x represents the phase at each measurement. We take a_0 from this model as the mean about which the variability occurs and report these as the average $\langle \mathrm{RV} \rangle$, $\langle T_{\rm eff} \rangle$, and $\langle \log(g) \rangle$ of the star. Table 2 contains a list of the best-fitting coefficients found for each data set.

RV calculations resulted in a peak-to-peak amplitude of 135 ± 5 km s^{-1} about a mean of 53.36 ± 1.44 km s^{-1} due to a large radius change throughout the pulsation cycle (see Section 4.2). The top panel of Fig. 2 shows the result of RV measurements made using both sets of Keck/ESI data taken approximately one year apart in 2020 July and 2021 June. The data points represent the average $\langle \mathrm{RV} \rangle$ of lines: H α, H β, H γ, H δ, and He I 4026, 4388, 4472, 4922, 5876, 6678 Å. Error bars for each point are included but small compared to the amplitude, only on the order of a few km s^{-1}. Both data sets were then phase folded on the period of 31.935 261 66(4) min. Note that there is no average radial velocity variation between the two epochs as would be likely if OGLE-BLAP-009 were in a binary orbit (see Section 4.3).

Table 2. List of best-fitting Fourier coefficients derived for RV, $T_{\rm eff}$, and $\log(g)$.

Coefficient	RV (km s^{-1})	$T_{\rm eff}$ (K)	$\log[g(\mathrm{cm\ s^{-2}})]$
a_0	53.36 ± 1.44	29 315.33 ± 331.36	4.38 ± 0.02
a_1	20.83 ± 2.01	2508.77 ± 448.43	0.13 ± 0.03
a_2	19.87 ± 2.07	−1433.19 ± 459.45	−0.02 ± 0.03
a_3	−12.88 ± 1.97	36.50 ± 459.22	0.04 ± 0.03
b_1	44.78 ± 2.05	−2856.67 ± 489.29	−0.08 ± 0.04
b_2	−14.47 ± 1.95	−427.03 ± 476.38	−0.14 ± 0.03
b_3	−3.37 ± 2.00	513.13 ± 461.15	0.08 ± 0.03

Atmospheric fittings using data collected from Keck/LRIS show a peak-to-peak $T_{\rm eff}$ variation of 10 868 ± 784 K about a mean of 29 315 ± 331 K and a peak-to-peak $\log(g)$ amplitude of 0.64 ± 0.01 about a mean of 4.38 ± 0.03 which can be seen in the middle and bottom panel of Fig. 2, respectively. These average measurements are consistent with results reported by Pietrukowicz et al. (2017). The phasing of these atmospheric fittings is such that at peak temperature the star is at maximum luminosity and $\log(g)$. This is an indication of the $T_{\rm eff}$ change as the predominant factor in flux variations seen in the light curve, which is also consistent with the phasing of the $g - r$ colour variations. Note that both $T_{\rm eff}$ and $\log(g)$ have a significantly higher measurement at their peak. We suspect that a shock is likely to trigger at minimum radius due to compression of the photosphere and travel outward through the outer layers of the stellar envelope, resulting in a spike of $T_{\rm eff}$ and $\log(g)$ that our spectral models may fail to adequately measure. Jeffery (2022) has recently shown for the example of the extreme helium star V652 Her that hydrostatic model spectra as used here can significantly deviate from a proper dynamical treatment at these phases.

3.3 Metal abundance analysis

The optical spectrum of OGLE-BLAP-009 shows unusually strong metal lines. In order to estimate the surface metal composition of OGLE-BLAP-009, we co-added the radial velocity-corrected ESI exposures least affected by the compression phase. The spectra used for this are marked blue in Fig. 2. We then constructed a TLUSTY/SYNSPEC model spectrum based on the previously derived low-$T_{\rm eff}$ phase atmospheric parameters, $\log g = 4.35$ and $\log y = -0.6$. Because He II 4686 Å is very sensitive to $T_{\rm eff}$, we used this line to estimate a best-fitting value of $T_{\rm eff} = 27\,250$ K for our metal line-blanketed model. The metal abundances were then iteratively adjusted to match the strong lines in the co-added ESI spectrum. In particular the many strong C II–III, N II–III, and O II–III lines are well matched by this model, as shown in the top panel of Fig. 3. Notable lines from heavier metals include Ne I 6143, 6402 Å, Ne II 4392, 4409 Å, the Mg II 4481 Å doublet, Al III 4150, 4480, 4529 Å, P III 4222, 4247 Å, as well as many Si III–IV, S III, and Fe III lines.

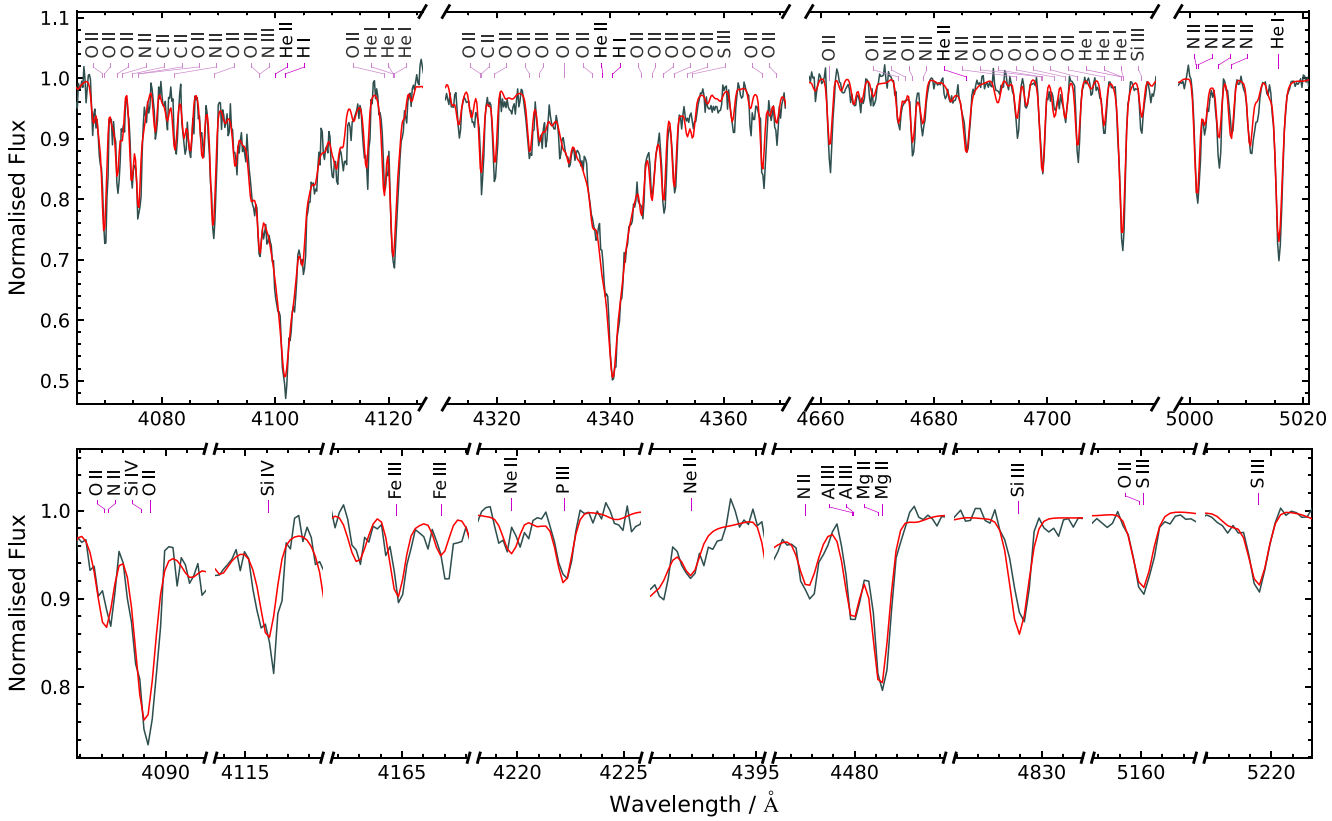

Figure 3. Example fittings of the synthetic TLUSTY/SYNSPEC model spectrum (red line) to the co-added radial-velocity corrected ESI spectra (black line) for notable metal lines. The model spectrum parameters are: $T_{\rm eff}$ = 27 250 K, $\log(g)$ = 4.35, $\log(y)$ = −0.6, and abundances as stated in Table 3.

Table 3. Surface abundances from the co-added ESI spectrum by number fraction $\varepsilon = n(\mathrm{X})/n(\mathrm{all})$ and compared to the solar values $\varepsilon_\odot$. Phases with the highest $T_{\rm eff}$ were not considered for the co-added spectrum. Both the abundances and uncertainties (68 per cent) were estimated by comparison with model spectra.

Element	$\log\varepsilon$	$\log\varepsilon/\varepsilon_\odot$
H	−0.10 ± 0.02	−0.06 ± 0.02
He	−0.70 ± 0.08	0.41 ± 0.08
C	−2.82 ± 0.10	0.79 ± 0.11
N	−2.80 ± 0.10	1.41 ± 0.11
O	−3.03 ± 0.10	0.32 ± 0.11
Ne	−3.41 ± 0.20	0.69 ± 0.23
Mg	−3.88 ± 0.10	0.56 ± 0.11
Al	−5.02 ± 0.10	0.56 ± 0.10
Si	−3.97 ± 0.15	0.56 ± 0.15
P	−5.96 ± 0.15	0.66 ± 0.15
S	−4.65 ± 0.10	0.27 ± 0.10
Fe	−3.89 ± 0.20	0.65 ± 0.20

Examples are shown in the bottom panel of Fig. 3. All of these metals were included in non-local thermodynamic equilibrium (non-LTE) using the largest model atoms distributed with TLUSTY 205 (Hubeny & Lanz 2017) with the exception of phosphorous, for which no good model atom is available. A full comparison between the co-added ESI spectrum and our best-fitting model is shown in Fig. A2.

All metal abundances turned out to be strongly enhanced when compared to solar values at factors between two and five; they are listed in Table 3. The especially strong enhancement in nitrogen, about 25 times solar by number fraction, is evidence for material processed by hydrogen fusion in the CN-cycle.

3.4 Spectral energy distribution

As a first photogeometric method in estimating the mass and radius of OGLE-BLAP-009, a spectral energy distribution (SED) fit was performed. This method is used to determine the angular diameter of the star and combine it with the *Gaia* EDR3 parallax to derive the stellar radius. The luminosity and mass are then calculated, making use of the atmospheric parameters determined from spectroscopy. This method was described in detail by Heber, Irrgang & Schaffenroth (2018). The $T_{\rm eff}$ and $\log(g)$ were fixed at 28 000 ± 1500 K and 4.40 ± 0.20 based on the results from spectroscopy which do not include measurements made during phases of compression and with uncertainties that accommodate the range of values caused by the pulsation cycle. Interstellar reddening was accounted for using the functions of Fitzpatrick et al. (2019), where the colour excess $E(44-55)$ was a free parameter and the extinction parameter $R(55)$ was fixed to the standard value of 3.02. Fig. 4 compares the best-fitting model spectrum to the available photometry. The radius was then calculated using $R = \Theta/2\varpi$, where Θ is the angular diameter estimated from the photometry and ϖ is the parallax measurement acquired from *Gaia* EDR3 (Gaia Collaboration 2021). The parallax uncertainty was inflated according to equation (16) of El-Badry, Rix & Heintz (2021) and a zero-point offset of −0.044 mas was applied following Lindegren et al. (2021). Rimoldini et al. (2022) classified the star as a variable of short period from *Gaia* DR3

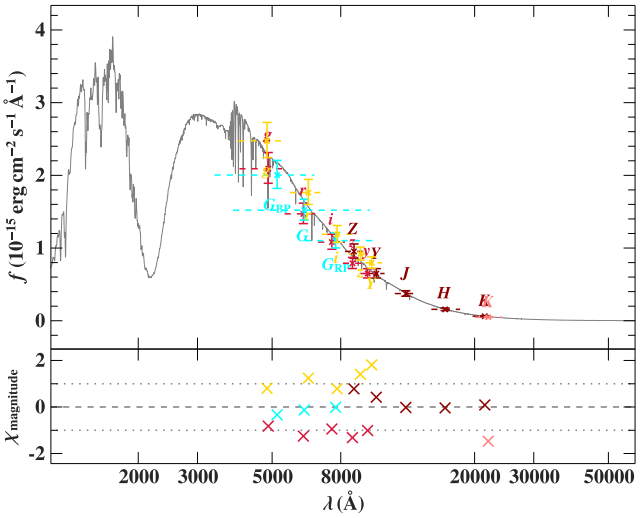

Figure 4. Spectral energy distribution fitting for OGLE-BLAP-009. The best-fitting model spectrum is shown as a grey line. Coloured data points represent flux measurements from different photometric surveys: *Gaia* (cyan, Riello et al. 2021), DECaPS (yellow, Schlafly et al. 2018), Pan-STARRS (red, Magnier et al. 2020), VISTA/VVV (dark red, Minniti et al. 2010), and UKIDSS (light red, Lucas et al. 2008).

Table 4. List of input parameters and results obtained from the SED.

Parameter	Value
Colour excess $E(44-55)$	0.670 ± 0.025 mag
Extinction parameter $R(55)$ (fixed)	3.02
Angular diameter $\log(\Theta\,(\mathrm{rad}))$	-10.942 ± 0.020
Parallax ϖ	0.46 ± 0.04 mas
Effective temperature $T_{\rm eff}$ (prescribed)	$28\,000 \pm 1500$ K
Surface gravity $\log(g\,(\mathrm{cm\,s^{-2}}))$ (prescribed)	4.40 ± 0.20
Helium abundance $\log(n(\mathrm{He}))$ (prescribed)	-0.60 ± 0.20
Radius $R = \Theta/(2\varpi)$	$0.55 \pm 0.06\,\mathrm{R}_\odot$
Mass $M = gR^2/G$	$0.28^{+0.19}_{-0.12}\,\mathrm{M}_\odot$
Luminosity $L/\mathrm{L}_\odot = (R/\mathrm{R}_\odot)^2(T_{\rm eff}/T_{\rm eff,\odot})^4$	170^{+60}_{-50}

photometry with Standard deviations of 0.091 and 0.074 mag in the *BP* and *RP* bands, respectively. The mass was then calculated using $M = gR^2/G$, where g is the surface gravity and G is the gravitational constant. These calculations resulted in a mass of $0.28^{+0.19}_{-0.12}$ $\mathrm{M}_\odot$ and a radius of 0.55 ± 0.06 $\mathrm{R}_\odot$. There is a large uncertainty on the mass in this case as a consequence of the uncertainty embedded in $\log(g)$ due to the radius change occurring during radial-mode pulsations.

Table 4 shows a list of all input parameters and results from the SED. Strong reddening can be seen in the photometry, due the location of OGLE-BLAP-009 in the Galactic Disc. The estimated luminosity using the $T_{\rm eff}$ input and derived radius corresponds to $\log(L/L_\odot) = 2.25^{+0.27}_{-0.20}$. This value is consistent with the derived luminosity from Pietrukowicz et al. (2017) for an approximately 0.30 $\mathrm{M}_\odot$ hydrogen shell-burning star with a degenerate helium-core.

3.5 Pulsation characteristics

In order to explore the pulsation characteristics of OGLE-BLAP-009, we utilized a variant of the Baade–Wesselink method, which is frequently applied to radial-mode pulsators to calculate stellar parameters (Baade 1926; Wesselink 1946). We make use of the phase-folded RV curve fitting from equation (1). Using this model,

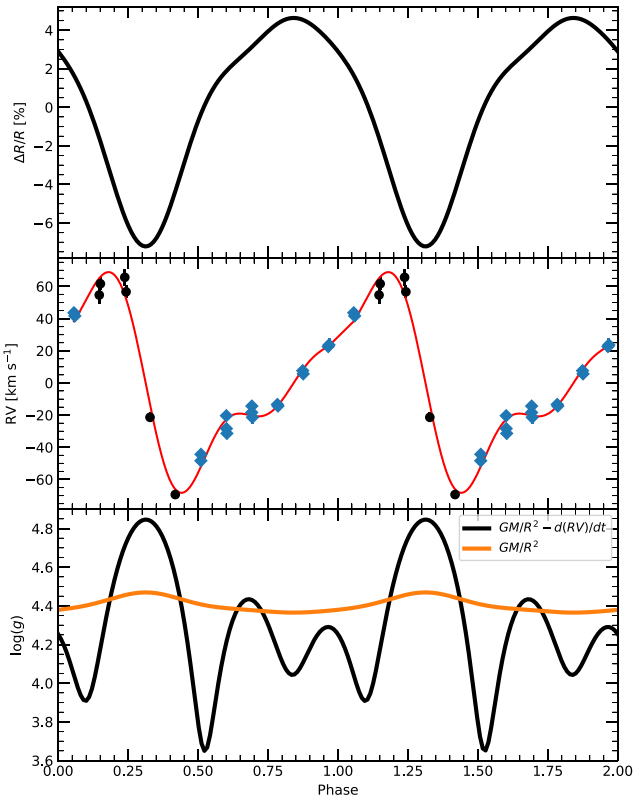

Figure 5. Pulsation properties calculated using a variant of the Baade–Wesselink method. Top panel: fractional radius change calculated using the integral of the RV fitting (equation 2), expressed as a per cent of the radius derived from the SED. Second panel: RV data points from Fig. 2 with the red line corresponding to the fitting model from equation (1). Bottom panel: acceleration calculated using the derivative of the RV fitting (black line) and the change in surface gravity calculated from the radius change (orange line).

we integrate and differentiate over the pulsation cycle to, respectively, find the radius change and surface gravity variations due to atmospheric acceleration. Fig. 5 displays the results of these calculations. Here, the top panel is the integral of the RV curve (equation 2) represented as a fractional radius change ($\Delta R/R$) relative to the radius derived from the SED and expressed as a per cent, such that a zero per cent variation occurs at 0.55 $\mathrm{R}_\odot$. The bottom panel shows the log of the superposition of the acceleration at the stellar surface and the underlying $\log(g)$ term ($\log(GM/R^2 - \mathrm{d(RV)/d}t)$) found from the derivative of the RV curve (black line), along with the change in surface gravity calculated from the change in radius alone ($\log(GM/R^2)$) using the radius and mass found from the SED calculation (orange line).

When integrating equation (1) over the pulsation cycle, it is necessary to adopt a projection factor to convert the measured radial velocities into true pulsation velocities. This factor takes into account a geometric projection due to limb darkening, a correction for the velocity gradient between the line forming regions and the photosphere, and relative motions between the gas and optical layers in the photosphere (see Nardetto et al. 2007; Guiglion et al. 2013). Following the works of Montañés Rodriguez & Jeffery (2001) and Barlow et al. (2010), we used a projection factor of $p = 1.4$ which was shown to be appropriate for sdB-type stars and where limb darkening is the main contribution to this value. We find that using equation (2), the amplitude of the radius change over the pulsation cycle of

OGLE-BLAP-009 is approximately 46 000 km.

$$\Delta R = -p \int_{t_0}^{t_f} \dot{r} \mathrm{d}t \tag{2}$$

In terms of the radius found using the SED fitting, this is a fractional radius change ($\Delta R/R$) of about 12 per cent. The phase at minimum radius corresponds to maximum $T_{\rm eff}$, $\log(g)$, and the photometric dip mentioned in Section 3.1, all of which occur at phase 0.31. The initial flux peak occurs just before minimum radius at phase 0.27.

Differentiating equation (1) shows the acceleration at the surface due to the velocity rate of change about the underlying surface gravity ($\log(GM/R^2 - \mathrm{dRV/d}t)$). The peak of this curve is in agreement with the peak surface gravity as seen from spectroscopy (Fig. 2). Note that the second peak in the observed $\log(g)$, as seen at phase 0.70 in the bottom panel of Fig. 2 is also present in the derived surface acceleration. This may be due to the change in velocity of the photosphere as it approaches its maximum radius, which can be seen as a flattening of the RV curve at this phase. To calculate the change of surface gravity coming from the radius fluctuation we use the mass derived from the SED and plot $\log(g)$ as a function of ΔR. This resulted in an additional $\log(g)$ change of 0.12 which is a less significant contribution to the overall change in spectroscopic $\log(g)$. Based on these results and the $\log(g)$ amplitude seen in the spectroscopic data, we conclude the predominant factor in this variation is the acceleration of the photosphere. This is an indication that hydrostatic modelling may lead to an improper treatment of the pressure broadening in the spectral lines and inaccurate $\log(g)$ measurements at phases of minimum radius.

4 DISCUSSION

4.1 Stellar evolution

In order to apply a secondary, independent method of estimating the mass and radius of OGLE-BLAP-009 and to place a constraint on its evolutionary history, a grid of theoretical models for He-core pre-WDs of masses between 0.29 and 0.35 $M_\odot$ were computed using MESA (Paxton et al. 2011, 2013, 2015, 2018, 2019). Additionally, linear adiabatic pulsation periods for both the fundamental and first-overtone radial modes were calculated for each step along these tracks using GYRE (Townsend & Teitler 2013). Fig. 6 shows OGLE-BLAP-009 plotted along with these models using the $T_{\rm eff}$ and $\log(g)$ from Section 3.4 with the period colour-mapped to the scale of first-overtone periods calculated using GYRE. The $T_{\rm eff}$ and $\log(g)$ of OGLE-BLAP-009 best matches that of a 0.33 $M_\odot$ He-core pre-WD. The GYRE period for the fundamental mode pulsation at this model's closest matching point is 2402.60 and 1900.60 s for the first overtone. Therefore, the observed period of ≈1916.12 s is best described by a first-overtone radial-mode pulsation using these models (see Fig. A1).

To calculate the radius and mass, a dimensionless frequency factor $f = \omega/\omega_{\rm dyn}$ was calculated for each point along the models' tracks, where ω is the mode frequency and $\omega_{\rm dyn} \equiv \sqrt{GM/R^3}$ is the stellar dynamical frequency. These factors from the best matching model are $f \approx 3.42$ for the fundamental radial-mode and $f \approx 4.31$ for the first-overtone radial mode. If the observed pulsation frequency corresponds to a radial-mode of frequency ω, then the radius and mass of the star can be calculated using the frequency factor f for that mode according to the following.

$$R = \frac{10^{\langle \log(g) \rangle} f^2}{\omega^2} \tag{3}$$

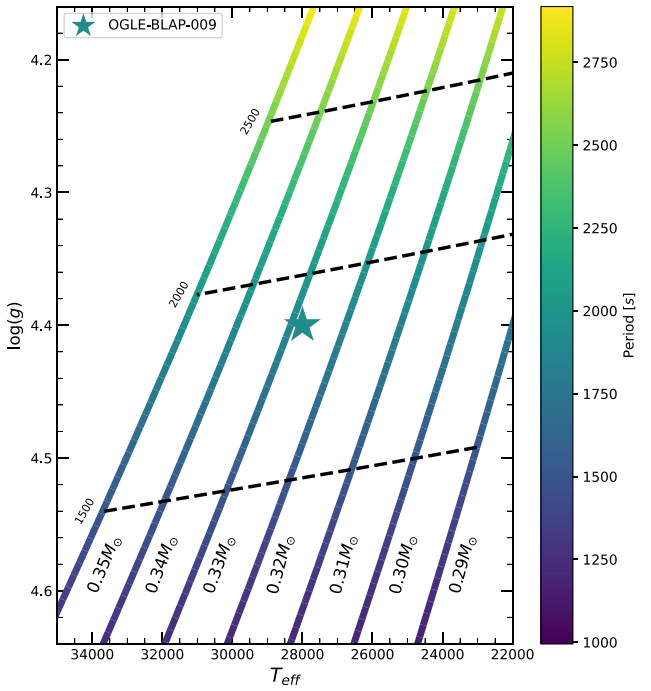

Figure 6. MESA evolution tracks in $T_{\rm eff} - \log(g)$ space for He-core pre-WDs of masses between 0.29 and 0.35 $M_\odot$ in steps of 0.01 $M_\odot$. The tracks are colour-mapped to the first-overtone radial-mode pulsation period calculated using GYRE along each step in the models' evolution. Period contours are also included as dashed black lines, which connect points of equal period across the models. OGLE-BLAP-009 is plotted using the mean $T_{\rm eff} - \log(g)$ acquired from spectroscopy and colour-mapped to the scale of pulsation periods with an observed period of ≈1916.12 s.

$$M = \frac{10^{\langle \log(g) \rangle} R^2}{G} = \frac{10^{\langle 3\log(g) \rangle} f^4}{G\omega^4} \tag{4}$$

Using equations (3) & (4) and the average surface gravity from Section 3.2, we calculate the mass and radius for an assumed fundamental radial-mode pulsation to be 0.14 ± 0.06 $M_\odot$ and 0.39 ± 0.07 $R_\odot$. For an assumed first-overtone pulsation, we calculate 0.36 ± 0.14 $M_\odot$ to be the mass and 0.63 ± 0.11 $R_\odot$ to be the radius. We find that the results calculated from the dynamical frequency of the first overtone show agreement with a low-mass He-core pre-WD which resembles the radius and mass found using the SED and *Gaia* parallax when considering the uncertainty caused by the changing photosphere. The period also closely resembles that of a predicted first-overtone pulsation at the mean $T_{\rm eff}$ and $\log(g)$ that we calculate from spectroscopy. The mass and radius calculated from this model is also more consistent with the predicted He-core pre-WD mass of 0.33 $M_\odot$. Although, due to uncertainty in $\log(g)$ the fundamental mode is not fully excluded. However, these calculations for OGLE-BLAP-009 clearly show consistency with a low-mass He-core pre-WD of ≈0.30 $M_\odot$.

4.2 Stellar pulsations

The pulsation features of OGLE-BLAP-009 are similar to the pulsating extreme helium stars V652 Her and BX Cir (Woolf & Jeffery 2002; Jeffery et al. 2015). Jeffery et al. (2015) conducted a line-by-line spectral analysis of V652 Her and found that the large radial-mode pulsations resulted in extreme compression of the photosphere at minimum radius. At this phase, the acceleration of individual ab-

sorption lines that are formed deeper in the stellar interior was shown to initiate before those formed closer to the surface. Their findings suggest that a shock wave propagates through the photosphere as the pulsation mechanism is triggered (Jeffery 2022; Jeffery, Montañés-Rodríguez & Saio 2022). Due to the short pulsation period of OGLE-BLAP-009 and the lack of spectra covering multiple phases of radius minimum, we do not attempt to resolve such variations in the phase of initial acceleration of the individual absorption lines. However, based on the rapid expansion and contraction of this star's radius, similar effects may be likely to occur.

The dip in flux occurring at maximum light may be a photometric indication of such a shock since it is present at the phase of minimum radius and stalls the flux decrease that occurs from radius expansion. The hydrodynamic pulsation models developed by Jeffery, Montañés-Rodríguez & Saio (2022), show that the flux from the immediate subsurface layers peaks shortly before the flux from the photosphere. This may be a reason for this photometric dip in flux and the phase delay between the first flux peak and minimum radius. The BLAP discovered by Pigulski, Kotysz & Kołaczek-Szymański (2022), which has a 32.37 min pulsation period also showed a similar feature in *TESS* 20-s cadence data occurring just after maximum flux. It was speculated by McWhirter, Lam & Steele (2020) that this double-peak feature could be the result of one peak corresponding to maximum temperature and the other maximum radius. This does not appear to be the case for OGLE-BLAP-009, as our phase-resolved results show that the point of maximum temperature occurs at the phase of minimum radius (see Section 3.5). Macfarlane et al. (2017) identified that this feature is similar to those found in 'Bump' Cepheid variables and is likely due to an exposure of the ionization shock front that is driving the pulsation as a result of the resonance between the fundamental and second-overtone pulsation modes. It is notable that these BLAPs which share this feature have a very similar pulsation period. This may be an indication that each of them share similar fundamental properties which result in the photometric presence of this feature.

The rapid variability in the observable properties of BLAPs creates the necessity for phase-resolved spectroscopy and proper spectral modelling. Both Jeffery et al. (2015) and Woolf & Jeffery (2002) emphasize the need for hydrodynamic models to best recover the true atmospheric properties of high-amplitude radially pulsating stars that are undergoing rapid changes of their radius. Jeffery (2022) has investigated the impact of these models on V625 Her and we identify the need for similar models in analysing BLAPs as well, based on the outlying $T_{\rm eff}$ and $\log(g)$ observed at minimum radius and the strong surface acceleration. Additionally, spectroscopic observations covering multiple pulsation cycles may help to determine the true maximum values as the phase smearing and lack of pulsation peaks covered by the spectra leads to uncertainties at minimum radius.

4.3 Radial velocity monitoring

If the evolutionary status for OGLE-BLAP-009 is best described as a He-core pre-WD, then a previous interaction with a binary companion through CEE or stable RLOF was responsible for the mass-loss of the BLAP progenitor (Byrne, Stanway & Eldridge 2021). This binary evolution channel implies that there may be an observable companion that can be detected through long-term radial velocity monitoring. We use the two Keck/ESI data sets to check if there is a variation in average ⟨RV⟩ about which the variability caused by stellar pulsations occurs. To quantify the mean radial velocity of each data set, both were phase folded and fitted individually with equation (1), keeping each constant fixed excluding a_0, representing the average ⟨RV⟩, which was left as an open parameter. This resulted

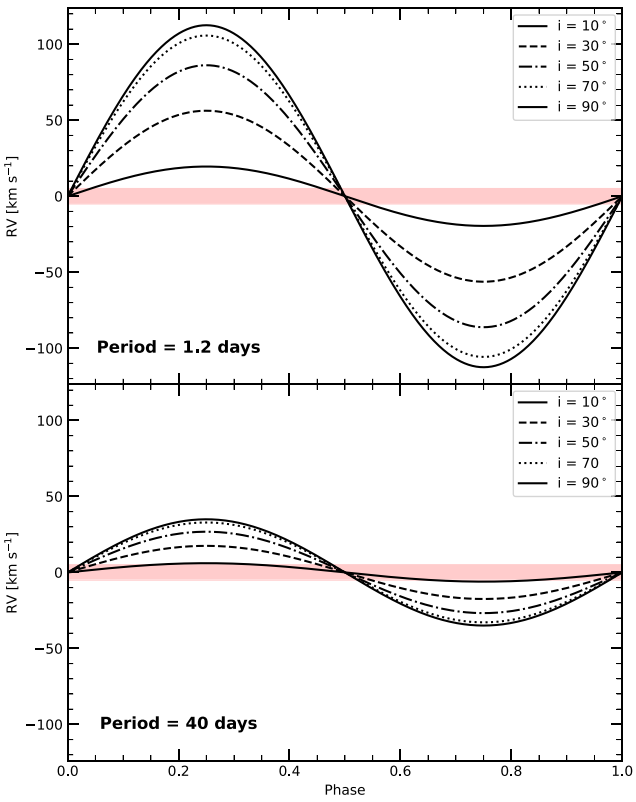

Figure 7. Radial velocity curve of possible binary orbits with various inclination angles, where OGLE-BLAP-009 is the secondary with an assumed mass of 0.34 $M_\odot$ and a low-mass main-sequence primary of 0.50 $M_\odot$. The top panel is an assumed short period of 1.2 d and the bottom panel is a longer period assumption of 40 d. The average ⟨RV⟩ is assumed to be zero and the region of uncertainty from the average ⟨RV⟩ measurement of each Keck/ESI data set is shaded in red, where a shift may be obscured.

in $a_0 = 54.44 \pm 1.84$ km s^{-1} for the 2020 July data set and $a_0 = 49.72 \pm 2.88$ km s^{-1} for 2021 June. An increase in uncertainty arises in the second data set since it covers less than one pulsation cycle. These results are the same within the uncertainty, however there is a range of ≈10 km s^{-1} in which an RV shift may be obscured.

Byrne, Stanway & Eldridge (2021) conducted a binary population synthesis study to determine which formation channels produce low-mass pre-WDs that possess observable properties of BLAPs. They find that 75 per cent of their BLAP models emerge as a result of RLOF where a low-mass main-sequence companion of ≈0.50 $M_\odot$ is responsible for the mass stripping of the BLAP progenitor in most cases. There is a bimodal distribution in the final orbital periods of these models with a small peak at 1.2 d and a larger peak at 40 d. Assuming a He-core pre-WD mass of 0.34 $M_\odot$ from the best matching MESA model and a companion of 0.50 $M_\odot$, we simulate radial velocity curves for both of these orbital periods. Fig. 7 shows these curves plotted for inclination angles between 10° and 90° in steps of 20°, centred about an average ⟨RV⟩ of zero with a region of uncertainty of ± 5 km s^{-1} shaded in red. Based off these assumptions, we find that a radial velocity shift for these binary orbits with inclination angles of <3° for the 1.2 d period and <10° for the 40 d period can be completely obscured. The probability of observing it at a phase within this obscured region decreases exponentially with inclination angle, down to an edge-on (90°) orbit. In this orientation a total time spent with a radial velocity amplitude of less than 10 km s^{-1} is 3 per cent of the orbit for a 1.2 d period and 9 per cent of the

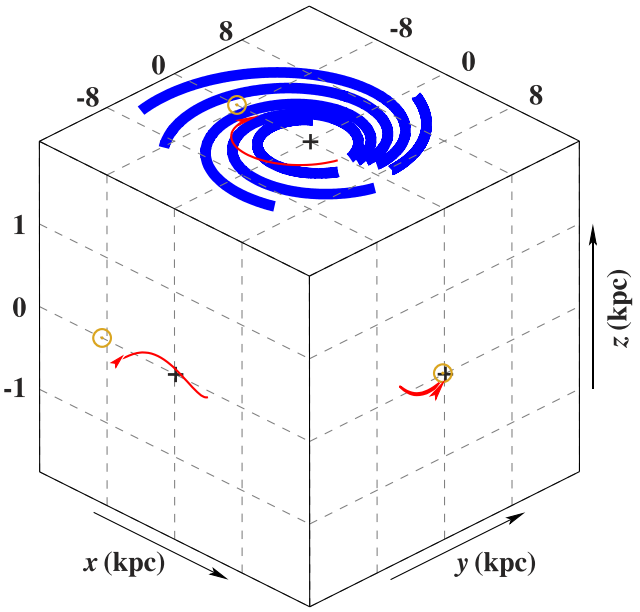

Figure 8. 3D Galactic orbit of OGLE-BLAP-009. The red line indicates the orbit of OGLE-BLAP-009 relative to the Galactic Plane (blue), Galactic Centre (plus), and Sun (yellow).

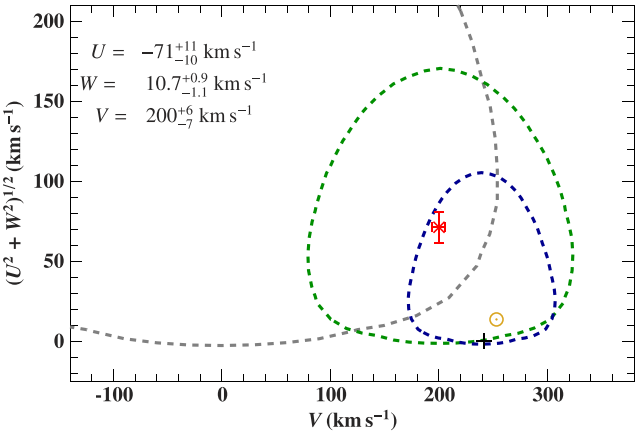

Figure 9. Toomre diagram for OGLE-BLAP-009 where the x-axis is the velocity in the direction of Galactic rotation (V), and the y-axis are the tangential velocities in the direction of the Galactic Centre (U) and Galactic North Pole (W), summed in quadrature. The blue, green, and grey dashed lines, respectively represent the 2σ contours for the thin disc, thick disc, and halo, based on data from Robin et al. (2003).

orbit for a 40 d period. It is therefore unlikely that an average ⟨RV⟩ shift would be missed, especially in the case of a short orbital period.

Using $O - C$ analysis of light-traveltime effects, Pigulski, Kotysz & Kołaczek-Szymański (2022) reported an approximate 23.084 33 d period of a BLAP around a late B-type main-sequence star in the binary system HD 133729. This constitutes the first BLAP discovered which lies in a confirmed binary system. If this BLAP shares a common origin with OGLE-BLAP-009, then it is possible that a binary orbital period would fall closer to the longer-period RV amplitude distributions, leading to a slightly increased probability of a non-detection of the companion. However, it is still unlikely that an average ⟨RV⟩ shift from an orbital period within this range would be missed at inclinations above 10°. Additionally, Pigulski, Kotysz & Kołaczek-Szymański (2022) show a decrease in the photometric pulsation amplitude of the BLAP due to light dilution from the bright companion, which is not present in OGLE-BLAP-009. Therefore, if a companion exists, it is likely a dim companion such as the one reported by Lin et al. (2023) from TMTS-BLAP1 results, and a longer orbital period is likely. This suggests that a proper $O - C$ analysis should be performed for OGLE-BLAP-009 and others like it in order to search for a binary companion.

4.4 Kinematics

The Galactic trajectory of OGLE-BLAP-009 was calculated as described in Irrgang et al. (2013) using their Galactic model potential I. This showed a usual orbit for a thin disc object with origins in the inner part of the disc. Fig. 8 shows its 3D Galactic orbit, relative to the Galactic Centre and Sun. This star stays within ≈100 pc of the Galactic Plane in the z direction, which is consistent with a thin disc object. However, the orbit is eccentric as can be seen in the x–y plane of Fig. 8. Fig. 9 shows a Toomre diagram for the space velocity of OGLE-BLAP-009. The eccentric orbit leads to it being settled on the bordering region between a thin disc (blue) and thick disc object (green). Tracing the orbit back 70 Myr, shows it originating from the inner part of the disc, ≈4 kpc from the centre. If the formation of OGLE-BLAP-009 occured in this region, this could be an explanation for the increased metallicity seen in Section 3.3. The high metallicity in combination with the strong nitrogen enrichment points to an intermediate mass main-sequence progenitor.

5 SUMMARY AND CONCLUSION

We present follow-up photometry and time-series spectroscopy of the blue large-amplitude pulsator OGLE-BLAP-009 in order to estimate the radius and mass of the star and place constraints on its evolutionary origins through comparison of its observed properties with theoretical models of He-core pre-WDs. We find large variability in flux, RV, $T_{\rm eff}$, and $\log(g)$ as a result of the rapid change in radius of about 12 per cent. We see no clear signs of a binary companion through photometry or through spectroscopy via an average ⟨RV⟩ shift between Keck/ESI data sets taken approximately one year apart. However, due to the uncertainty in ⟨RV⟩ we cannot rule out any binary orbits that would result in a radial velocity shift of less than 10 km s^{-1}.

A spectral energy distribution fitting of available photometric flux measurements to hot subdwarf models, combined with the *Gaia* parallax and using the $T_{\rm eff}$ and $\log(g)$ derived from spectroscopy resulted in a mass of $0.28^{+0.19}_{-0.12}$ M$_\odot$ and radius of 0.55 ± 0.06 R$_\odot$. Placing OGLE-BLAP-009 on a $T_{\rm eff}$ – $\log(g)$ diagram along with evolution tracks of He-core pre-WDs computed using MESA showed a close match with the model of mass 0.33 M$_\odot$. Predicted periods of fundamental and first-overtone radial-mode pulsations were calculated for each model using GYRE and the observed period best matched that of the first-overtone radial mode. Calculating the mass and radius using a dynamical frequency factor of the closest matching model in period, $T_{\rm eff}$, and $\log(g)$ for the first-overtone mode resulted in a mass of 0.36 ± 0.14 M$_\odot$ and radius of 0.63 ± 0.11 $R_\odot$ which is consistent with the SED results.

Our study indicates that the observed properties of OGLE-BLAP-009 can best be explained by a low-mass He-core pre-WD of ≈0.30 M$_\odot$. There are uncertainties in the mass estimates due to the change in surface gravity caused by stellar pulsations, but the results show a clear constraint to an evolutionary scenario that results in a low-mass object of less than 0.50 M$_\odot$. Further photometric analysis of the observed light-curve peaks over time may help to confirm if

OGLE-BLAP-009 is, in fact, in a binary orbit. Using $O - C$ analysis of pulse timing measurements can reveal orbital reflex motion due to light-traveltime effects. This has proven useful in the study of the only two BLAPs discovered to be in a binary system, HD 133 729 and TMTS-BLAP1 (Pigulski, Kotysz & Kołaczek-Szymański 2022; Lin et al. 2023). Confirming binary orbits in BLAPs and high-gravity BLAPs will help in constraining evolutionary channels that lead to their formation. The results presented here show that this method of analysis will prove useful if applied to other BLAPs in order to characterize their observable properties and attempt to place constraints on their evolutionary history. Additional spectroscopic observations are currently underway in order to apply this analysis to a statistically significant sample and determine if the class of BLAPs as a whole share similar characteristics and evolutionary status.

ACKNOWLEDGEMENTS

We thank Andreas Irrgang for the development of the spectrum and spectral energy distribution fitting tools and his contributions to the model atmosphere grids. BNB acknowledges support from National Science Foundation award AST 1812874. TK acknowledges support from the National Science Foundation through grant AST 2107982, from NASA through grant 80NSSC22K0338 and from STScI through grant HST-GO-16659.002-A. This work was supported, in part, by the National Science Foundation through grant PHY-1748958, and by meetings supported by the Gordon and Betty Moore Foundation through grant GBMF5076. Co-funded by the European Union (ERC, CompactBINARIES, 101078773). Views and opinions expressed are however those of the author(s) only and do not necessarily reflect those of the European Union or the European Research Council. Neither the European Union nor the granting authority can be held responsible for them.

This work has made use of data from the European Space Agency (ESA) mission *Gaia* (https://www.cosmos.esa.int/gaia), processed by the *Gaia* Data Processing and Analysis Consortium (DPAC, https://www.cosmos.esa.int/web/gaia/dpac/consortium). Funding for the DPAC was provided by national institutions, in particular the institutions participating in the *Gaia* Multilateral Agreement.

DATA AVAILABILITY

The spectroscopic data taken with Keck/LRIS and Keck/ESI can be downloaded from the Keck archive. The photometric data used in this paper will be provided upon request.

REFERENCES

Baade W., 1926, Astron. Nachr., 228, 359
Barlow B. N. et al., 2010, MNRAS, 403, 324
Byrne C. M., Jeffery C. S., 2018, MNRAS, 481, 3810
Byrne C. M., Jeffery C. S., 2020, MNRAS, 492, 232
Byrne C. M., Stanway E. R., Eldridge J. J., 2021, MNRAS, 507, 621
Córsico A. H., Althaus L. G., Serenelli A. M., Kepler S. O., Jeffery C. S., Corti M. A., 2016, A&A, 588, A74
Córsico A. H., Romero A. D., Althaus L. G., Pelisoli I., Kepler S. O., 2018, preprint (arXiv:1809.07451)
Dorsch M., Jeffery C. S., Irrgang A., Woolf V., Heber U., 2021, A&A, 653, A120
El-Badry K., Rix H.-W., Heintz T. M., 2021, MNRAS, 506, 2269
Fitzpatrick E. L., Massa D., Gordon K. D., Bohlin R., Clayton G. C., 2019, ApJ, 886, 108
Gaia Collaboration, 2016, A&A, 595, A1
Gaia Collaboration, 2018, A&A, 616, A1
Gaia Collaboration, 2021, A&A, 649, A1
Geier S. et al., 2011, A&A, 530, A28
Guiglion G. et al., 2013, A&A, 550, L10
Heber U., 1986, A&A, 155, 33
Heber U., 2009, ARA&A, 47, 211
Heber U., 2016, PASP, 128, 082001
Heber U., Irrgang A., Schaffenroth J., 2018, Open Astron., 27, 35
Hirsch H. A., 2009, PhD thesis, Friedrich Alexander Univ. Erlangen-Nuremberg, Germany
Hubeny I., Lanz T., 2017, preprint (arXiv:1706.01859)
Irrgang A., Wilcox B., Tucker E., Schiefelbein L., 2013, A&A, 549, A137
Jeffery C. S., 2022, MNRAS, 515, 716
Jeffery C. S., Kurtz D., Shibahashi H., Starling R. L. C., Elkin V., Montañés-Rodríguez P., McCormac J., 2015, MNRAS, 447, 2836
Jeffery C. S., Montañés-Rodríguez P., Saio H., 2022, MNRAS, 509, 1940
Kupfer T. et al., 2019, ApJ, 878, L35
Lenz P., Breger M., 2005, Commun. Asteroseismol., 146, 53
Lin J. et al., 2023, Nat. Astron., 7, 223
Lindegren L. et al., 2021, A&A, 649, A4
Lucas P. W. et al., 2008, MNRAS, 391, 136
Macfarlane S. A. et al., 2017, MNRAS, 465, 434
Magnier E. A. et al., 2020, ApJS, 251, 6
McWhirter P. R., Lam M. C., 2022, MNRAS, 511, 4971
McWhirter P. R., Lam M. C., Steele I. A., 2020, MNRAS, 496, 1105
Meng X.-C., Han Z.-W., Podsiadlowski P., Li J., 2020, ApJ, 903, 100
Minniti D. et al., 2010, New Astron., 15, 433
Montañés Rodriguez P., Jeffery C. S., 2001, A&A, 375, 411
Napiwotzki R., Karl C. A., Lisker T., Heber U., Christlieb N., Reimers D., Nelemans G., Homeier D., 2004, Ap&SS, 291, 321
Nardetto N., Mourard D., Mathias P., Fokin A., Gillet D., 2007, A&A, 471, 661
Oke J. B. et al., 1995, PASP, 107, 375
Paxton B., Bildsten L., Dotter A., Herwig F., Lesaffre P., Timmes F., 2011, ApJS, 192, 3
Paxton B. et al., 2013, ApJS, 208, 4
Paxton B. et al., 2015, ApJS, 220, 15
Paxton B. et al., 2018, ApJS, 234, 34
Paxton B. et al., 2019, ApJS, 243, 10
Perley D. A., 2019, PASP, 131, 084503
Pietrukowicz P. et al., 2017, Nat. Astron., 1, 0166
Pigulski A., Kotysz K., Kołaczek-Szymański P. A., 2022, A&A, 663, A62
Ramsay G. et al., 2022, MNRAS, 513, 2215
Riello M. et al., 2021, A&A, 649, A3
Rimoldini L. et al., 2022, A&A, 674, A14
Robin A. C., Reylé C., Derrière S., Picaud S., 2003, A&A, 409, 523
Romero A. D., Córsico A. H., Althaus L. G., Pelisoli I., Kepler S. O., 2018, MNRAS, 477, L30
Schlafly E. F. et al., 2018, ApJS, 234, 39
Sheinis A. I., Bolte M., Epps H. W., Kibrick R. I., Miller J. S., Radovan M. V., Bigelow B. C., Sutin B. M., 2002, PASP, 114, 851
Townsend R. H. D., Teitler S. A., 2013, MNRAS, 435, 3406
Udalski A., Szymański M. K., Szymański G., 2015, Acta Astron., 65, 1
Wesselink A. J., 1946, Bull. Astron. Inst. Netherlands, 10, 91
Woolf V. M., Jeffery C. S., 2002, A&A, 395, 535
Wu T., Li Y., 2018, MNRAS, 478, 3871
Xiong H. et al., 2022, A&A, 668, A112

APPENDIX A: ADDITIONAL FIGURES

Fig. A1 shows a comparison between the pulsation period match of OGLE-BLAP-009 to the periods calculated for the fundamental and first-overtone radial modes. The period of OGLE-BLAP-009 more closely matches the predicted period for a first-overtone pulsation at the mean $T_{\rm eff}$ and $\log(g)$ derived from spectroscopy. Fig. A2 shows a full comparison between the co-added ESI spectrum and our best-fitting TLUSTY/SYNSPEC model.

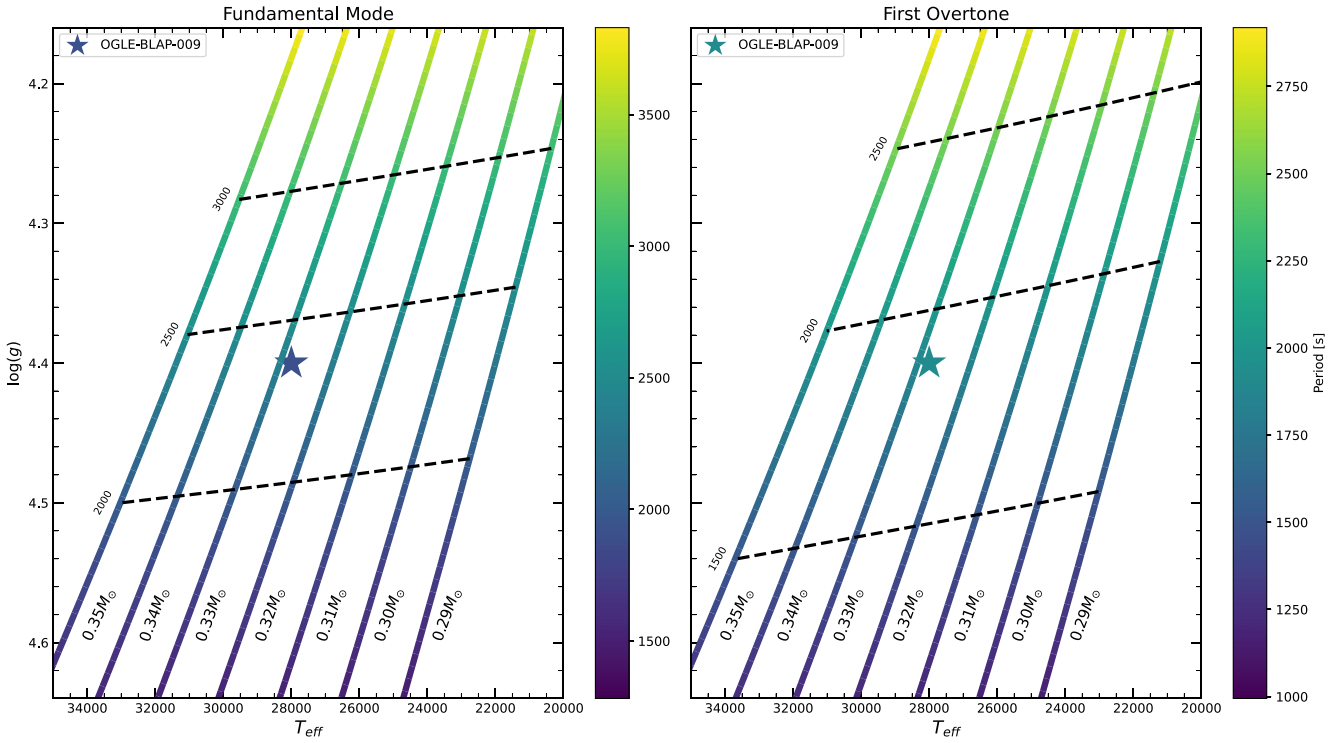

Figure A1. A comparison of the GYRE fundamental and first-overtone radial-mode pulsation periods matched to the observed period of OGLE-BLAP-009 at ≈1916.12 s. Left panel: MESA He-core pre-WD $T_{\rm eff} - \log(g)$ models colour-mapped to the fundamental radial-mode GYRE periods. Right panel: the same MESA models colour-mapped to the first-overtone radial-mode GYRE periods. Period contours are also included for each panel as dashed black lines, which connect points of equal period across the models.

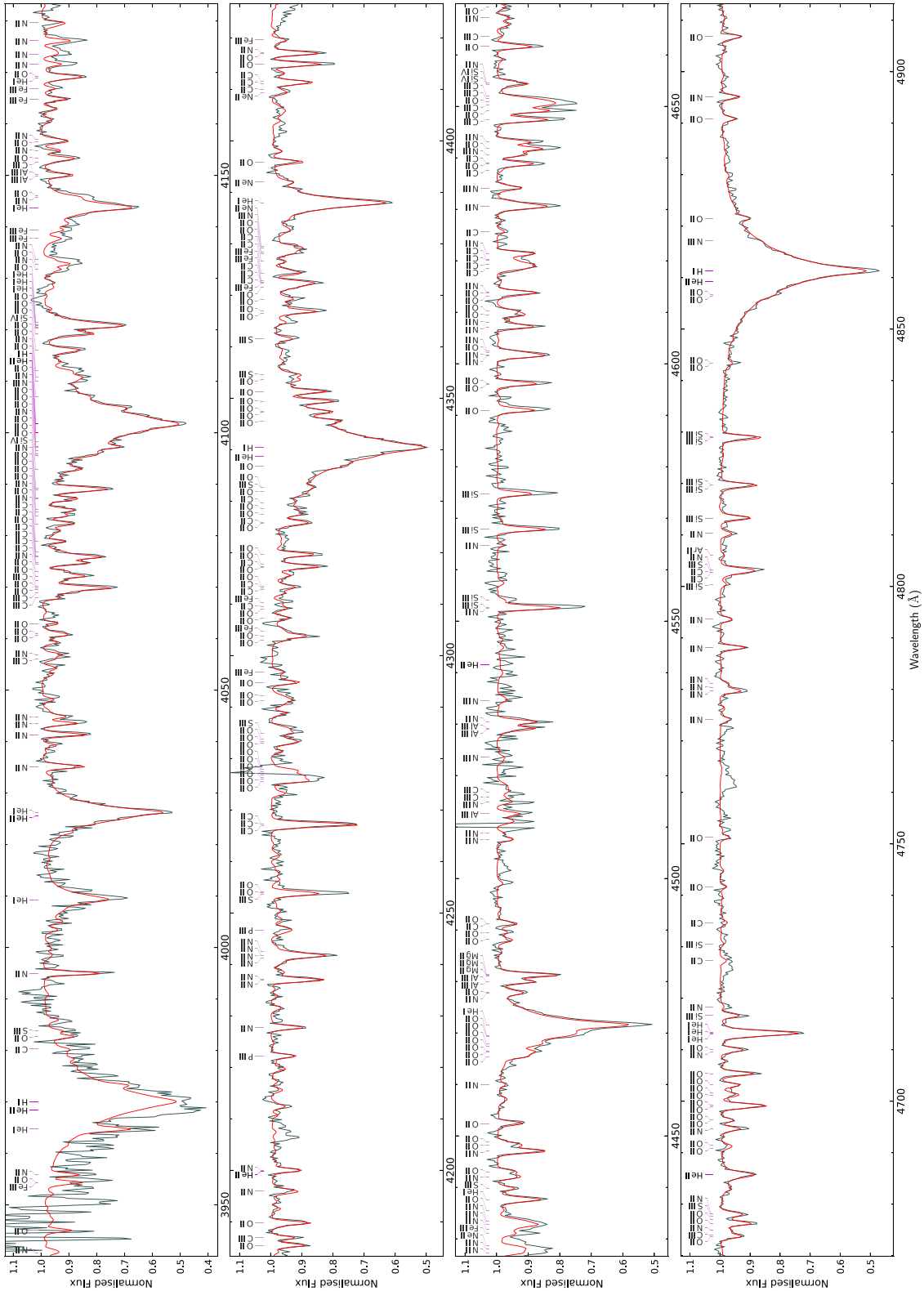

Figure A2. Co-added ESI spectrum of OGLE-BLAP-009 (grey) and the final model (red).

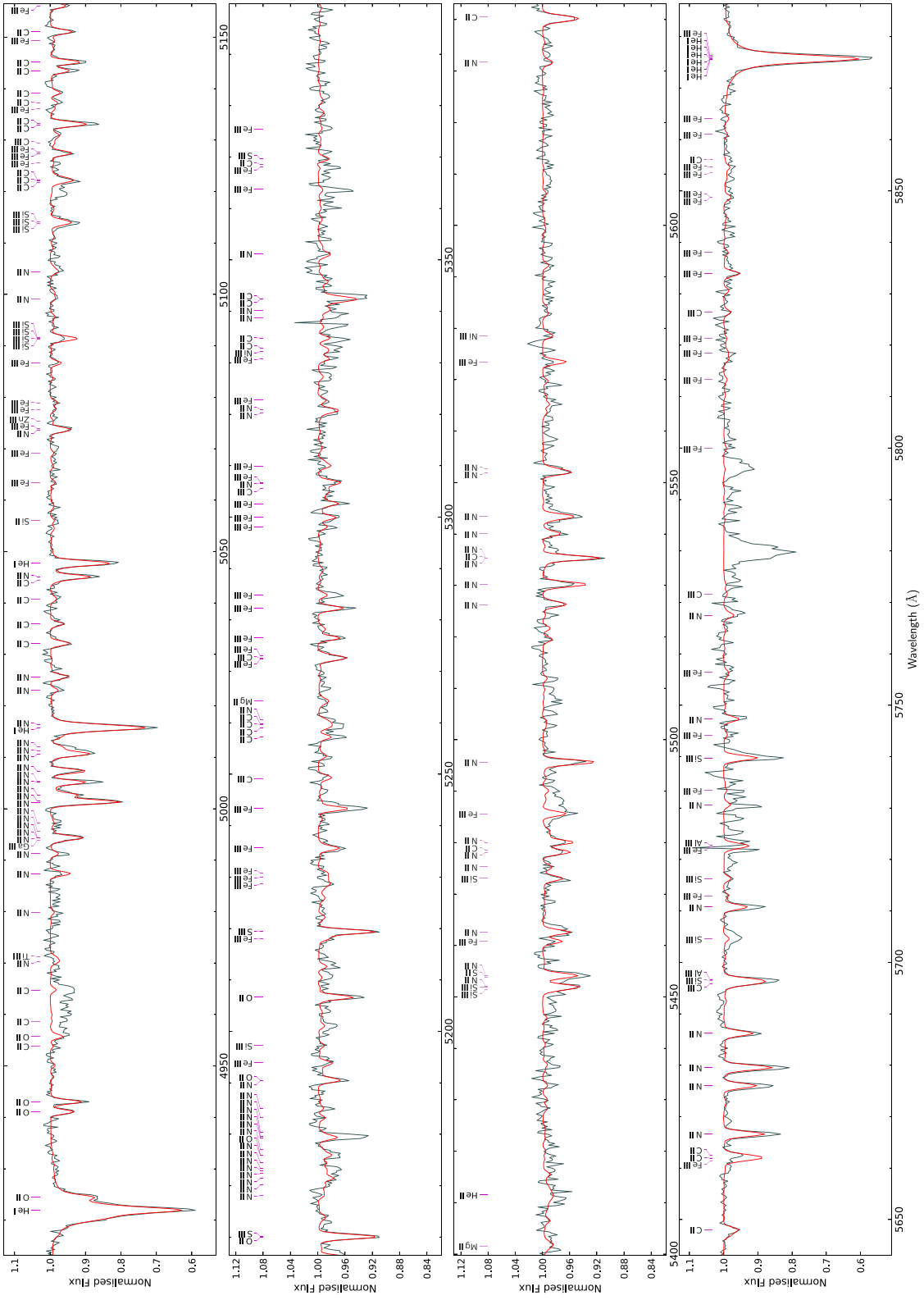

Figure A2. (*Continued.*)

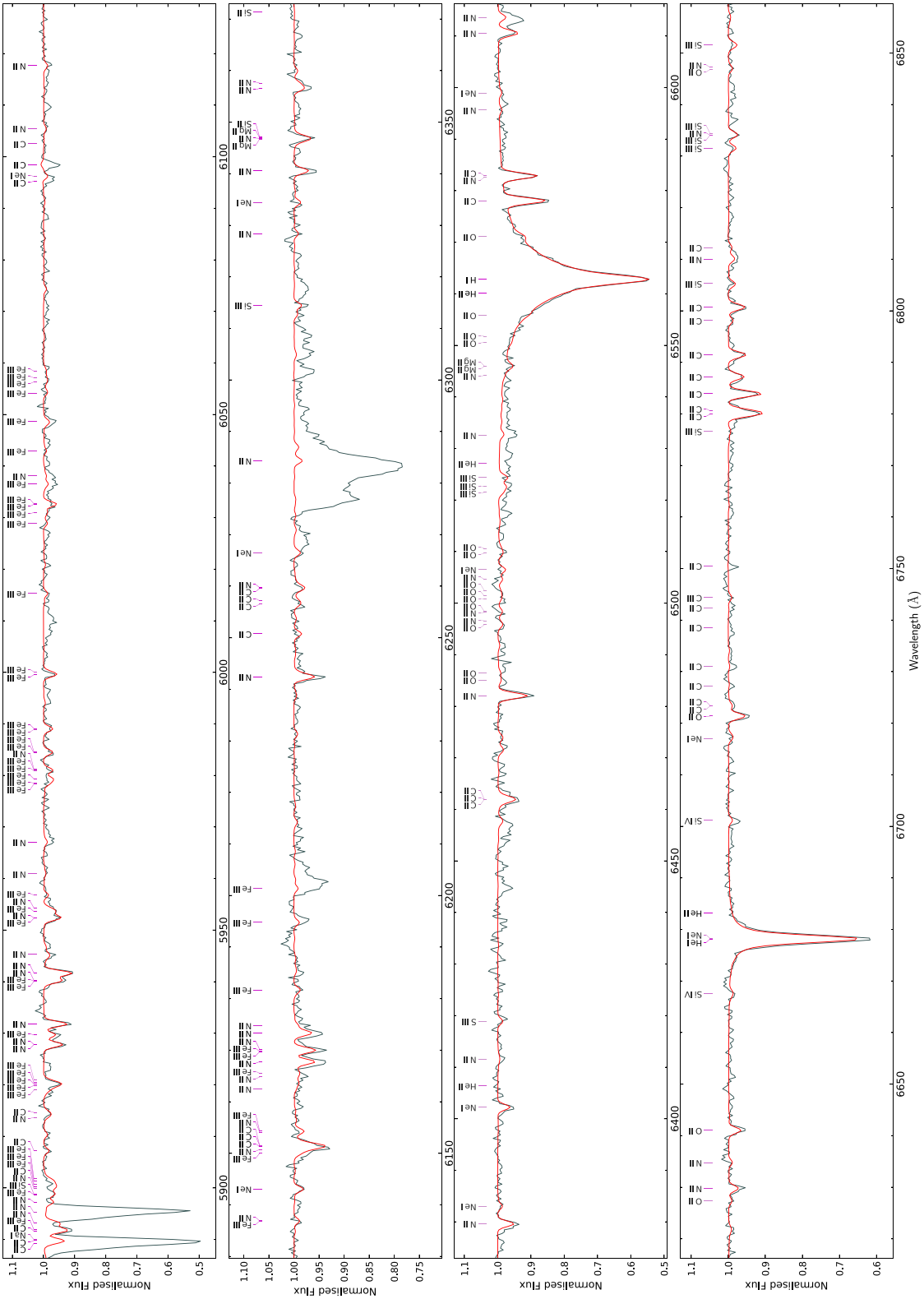

Figure A2. (*Continued.*)

APPENDIX B: TABLE OF VALUES FROM PHASE-RESOLVED SPECTROSCOPY

Table B1. List of values from phase-resolved spectroscopy. The instrument used and date of acquisition are available for each data point. Corresponding uncertainties for each measurement are included, which are statistically small, only on the order of 1σ.

Instrument	Date	Phase	RV (km s^{-1})	$T_{\rm eff}$ (K)	log (g)	log (y)
ESI	2020 July	0.056 339 67	97 ± 3	–	–	–
ESI	2021 June	0.059 576 54	95 ± 4	–	–	–
LRIS	2021 Sept.	0.069 879 98	–	27 290 ± 633	4.34 ± 0.08	−0.68 ± 0.12
ESI	2020 July	0.146 833 26	108 ± 5	–	–	–
ESI	2021 June	0.150 842 99	115 ± 4	–	–	–
LRIS	2021 Sept.	0.151 847 87	–	27 937 ± 612	4.43 ± 0.08	−0.73 ± 0.15
LRIS	2021 Sept.	0.233 815 77	–	30 209 ± 1219	4.51 ± 0.09	−0.47 ± 0.11
ESI	2020 July	0.238 093 38	119 ± 5	–	–	–
ESI	2021 June	0.242 696 05	110 ± 4	–	–	–
LRIS	2021 Sept.	0.315 558 22	–	36 660 ± 558	4.80 ± 0.05	−0.74 ± 0.13
ESI	2020 July	0.328 316 41	32 ± 3	–	–	–
LRIS	2021 Sept.	0.397 526 12	–	32 959 ± 1250	4.50 ± 0.10	−0.63 ± 0.11
ESI	2020 July	0.418 5399	−16 ± 2	–	–	–
LRIS	2021 Sept.	0.479 494 01	–	32 226 ± 865	4.30 ± 0.05	−0.56 ± 0.08
ESI	2020 July	0.510 176 29	5 ± 2	–	–	–
ESI	2020 July	0.510 3862	9 ± 2	–	–	–
LRIS	2021 Sept.	0.561 461 88	–	30 207 ± 676	4.27 ± 0.08	−0.66 ± 0.16
ESI	2020 July	0.601 150 32	33 ± 2	–	–	–
ESI	2020 July	0.601 210 95	25 ± 2	–	–	–
ESI	2021 June	0.603 062 64	22 ± 2	–	–	–
LRIS	2021 Sept.	0.643 7003	–	28 357 ± 868	4.47 ± 0.08	−0.78 ± 0.14
LRIS	2021 Sept.	0.659 769 97	–	27 114 ± 752	4.26 ± 0.09	−0.53 ± 0.12
ESI	2020 July	0.691 975 09	35 ± 3	–	–	–
ESI	2020 July	0.692 185	39 ± 3	–	–	–
ESI	2021 June	0.694 104 06	32 ± 4	–	–	–
LRIS	2021 Sept.	0.725 397 66	–	27 775 ± 679	4.51 ± 0.08	−0.67 ± 0.10
LRIS	2021 Sept.	0.741 737 86	–	27 494 ± 712	4.51 ± 0.08	−0.72 ± 0.12
ESI	2020 July	0.783 505 75	40 ± 3	–	–	–
ESI	2021 June	0.785 686 15	39 ± 3	–	–	–
LRIS	2021 Sept.	0.807 365 55	–	25 792 ± 551	4.20 ± 0.09	−0.62 ± 0.10
LRIS	2021 Sept.	0.823 705 76	–	28 222 ± 664	4.29 ± 0.07	−0.59 ± 0.11
ESI	2020 July	0.873 999 33	61 ± 2	–	–	–
ESI	2021 June	0.875 915 94	59 ± 3	–	–	–
LRIS	2021 Sept.	0.889 333 44	–	26 473 ± 715	4.16 ± 0.08	−0.52 ± 0.10
LRIS	2021 Sept.	0.905 673 67	–	26 056 ± 891	4.18 ± 0.07	−0.50 ± 0.10
ESI	2020 July	0.965 034 46	76 ± 3	–	–	–
ESI	2021 June	0.967 994 02	77 ± 4	–	–	–
LRIS	2021 Sept.	0.987 641 57	–	26 311 ± 567	4.18 ± 0.09	−0.60 ± 0.14

This paper has been typeset from a TEX/LATEX file prepared by the author.